

1 INTRODUCTION

2 Above Earth's atmosphere are the Van Allen radiation belts, a toroidally-shaped
3 pair of belts that consist of a complex and dynamic plasma environment. The inner
4 radiation belt is stable, consists of mostly energetic protons, and is located within 2
5 Earth radii (measured near the equator) above Earth's surface. The outer radiation
6 belt, on the other hand, consists of mostly energetic electrons, is highly dynamic
7 on day and hour time scales, and is typically found between 4 and 8 Earth radii
8 above Earth's surface. These belts pose a threat to space exploration due to their
9 adverse effects on our bodies and electrical components. A few **effects** include: a
10 high radiation dose for manned missions, degradation of silicon that causes transistor
11 malfunction, computer memory corruption due to bit flips, etc. With these effects in
12 mind, it is no surprise that the radiation belts have been extensively studied since
13 their discovery in the 1960s.

14 The radiation belt particles, mostly consisting of electrons and protons, are at
15 times unstable to wave growth and generate electric and magnetic waves. These
16 waves can then accelerate and scatter radiation belt particles with a variety of wave-
17 particle mechanisms. These wave-particle interactions are believed to be responsible
18 for scattering electron microbursts, a short and intense increase of precipitating
19 electrons into Earth's atmosphere, that are capable of destroying ozone molecules
20 and rapidly deplete the outer belt's electrons.

21 Electron microbursts, henceforth referred to as microbursts, are typically
22 observed by low Earth orbiting spacecraft, sounding rockets, and high altitude
23 balloons as a sub-second impulse of electrons. Some of the most intense microbursts
24 have electron fluxes that are a factor of 10 to 100 above the background (for example
25 see Fig. 7 in Blake et al. (1996)). Since they were first reported by Anderson and

26 Milton (1964), the intense transient nature of microbursts have compelled countless
27 researchers to pursue an understanding of their properties, their effects on the
28 environment, and the physical mechanism(s) that create microbursts. Microbursts
29 are widely believed to be created by wave-particle scattering between a plasma wave
30 called whistler mode chorus and outer radiation belt electrons, although many details
31 regarding the scattering mechanism are unconstrained or unknown. The goal of this
32 dissertation is to expand our knowledge of the wave-particle scattering mechanism
33 that scatters electron microbursts.

34 This chapter serves as an introduction to the fundamental physical concepts
35 that are essential to understand wave-particle interactions in Earth's magnetosphere.
36 We will review the motion of charged particles in electric and magnetic fields, how
37 particles are organized in the magnetosphere, how particles are accelerated and lost in
38 the magnetosphere, and review the current state of our understanding of microbursts.

39 Then the rest of this dissertation expands our knowledge of microbursts. In
40 Chapter ?? (chapter numbers will be filled in the full dissertation) we will investigate
41 and model the scattering mechanism responsible for microbursts observed inside the
42 outer radiation belt, near the magnetic equator. Then in Chapters ?? and ?? we
43 will investigate the microburst scattering mechanism indirectly by estimating the
44 microburst footprint size in low Earth orbit and the magnetic equator (near where
45 microburst electrons are believed to be scattered) and compare it to sizes of chorus
46 waves estimated in prior literature.

47 Charged Particle Motion in Electric and Magnetic Fields

A charged particle trapped in the magnetosphere will experience three types of periodic motion in Earth's nearly dipolar magnetic field in the absence of electric fields. The three motions are ultimately due to the Lorentz force that a particle of

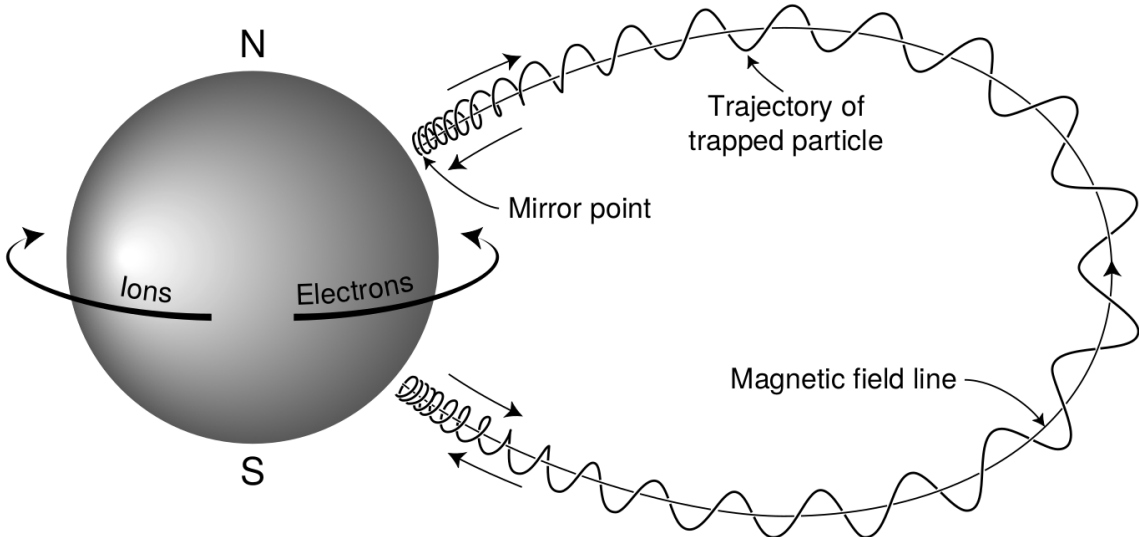


Figure 1.1: The three periodic motions of charged particles in Earth's dipole magnetic field. These motions are: gyration about the magnetic field line, bounce motion between the magnetic poles, and azimuthal drift around the Earth. Figure from (Baumjohann and Treumann, 1997).

momentum \vec{p} , charge q , and velocity \vec{v} experiences in an electric field \vec{E} and magnetic field \vec{B} and is given by

$$\frac{d\vec{p}}{dt} = q(\vec{E} + \vec{v} \times \vec{B}). \quad (1.1)$$

- ⁴⁸ In the magnetosphere, the three periodic motions, in decreasing frequency, are
- ⁴⁹ gyration, bounce, and drift and are schematically shown in Fig. 1.1. Each periodic
- ⁵⁰ motion has a corresponding conserved quantity i.e. an adiabatic invariant.

The highest frequency periodic motion is gyration about a magnetic field of magnitude B . This motion is circular with a Larmor radius of

$$r = \frac{mv_{\perp}}{|q|B} \quad (1.2)$$

where m is the mass and v_{\perp} the particle's velocity perpendicular to \vec{B} . This motion

has a corresponding gyrofrequency of

$$\Omega = \frac{|q|B}{m} \quad (1.3)$$

in units of radians/second. In the radiation belts, the electron gyrofrequency, Ω_e , is on the order of a kHz. The corresponding adiabatic invariant is found by integrating the particle's canonical momentum around the particle's path of gyration,

$$J_i = \oint (\vec{p} + q\vec{A}) \cdot d\vec{l} \quad (1.4)$$

where J_i is the i^{th} adiabatic invariant and \vec{A} is the magnetic vector potential. This integral is carried out by integrating the first term over the circumference of the gyro orbit and integrating the second term using Stokes theorem to calculate the magnetic flux enclosed by the gyro orbit. The gyration invariant is $J_1 \sim v_\perp^2/B$ which is conserved when the frequency, ω , of a force acting on the gyrating electron satisfies

$$\omega \ll \Omega_e.$$

The second highest frequency periodic motion is bouncing due to a parallel gradient in \vec{B} . This periodic motion naturally arises in the magnetosphere because Earth's magnetic field is stronger near the poles. To understand this motion we first we need to define the concept of pitch angle, α as the angle between \vec{B} and \vec{v} which is schematically shown in Fig. 1.2a. The pitch angle relates v with v_\perp and $v_{||}$, the component of the particles velocity parallel to \vec{B} . As shown in Fig. 1.2b and 1.2c, a smaller (larger) α will increase (decrease) the distance that the charged particle travels parallel to \vec{B} during one gyration.

Assuming the particle's kinetic energy is conserved, the conservation of J_1 implies that given a particle's $v_\perp(0)$ and $B(0)$ at the magnetic equator (where Earth's magnetic field is usually at a minimum) we can calculate its $v_\perp(s)$ along

the particle's path, s , by calculating $B(s)$ from magnetic field models. Thus the particle's perpendicular velocity is then related via

$$\frac{v_{\perp}^2(0)}{B(0)} = \frac{v_{\perp}^2(s)}{B(s)} \quad (1.5)$$

⁶⁵ which can be rewritten as

$$\frac{v^2 \sin^2 \alpha(0)}{B(0)} = \frac{v^2 - v_{\parallel}^2(s)}{B(s)} \quad (1.6)$$

⁶⁶ and re-arranged to solve for $v_{\parallel}(s)$ by

$$v_{\parallel}(s) = v \sqrt{1 - \frac{B(s)}{B(0)} \sin^2 \alpha(0)} \quad (1.7)$$

⁶⁷ which will tend towards 0 as the second term in the radical approaches 1.

⁶⁸ The location where $v_{\parallel}(s) = 0$ is called the mirror point and is where a particle
⁶⁹ reverses direction. Since Earth's magnetic field is stronger towards the poles, the
⁷⁰ mirroring particle will execute periodic bounce motion between its two mirror points
⁷¹ in the northern and southern hemispheres. The corresponding adiabatic invariant, J_2
⁷² is

$$J_2 = \oint p_{\parallel} ds \quad (1.8)$$

where ds describes the particle path between the mirror points in the northern and southern hemispheres (see Fig. 1.1). J_2 is found by substituting Eq. 1.7 into Eq. 1.8 and defining the magnetic field strength at the mirror points as B_m (where $\alpha(m) = 90^\circ$). The J_2 integral can be written as

$$J_2 = 2p \int_{m_n}^{m_s} \sqrt{1 - \frac{B(s)}{B(m)}} ds \quad (1.9)$$

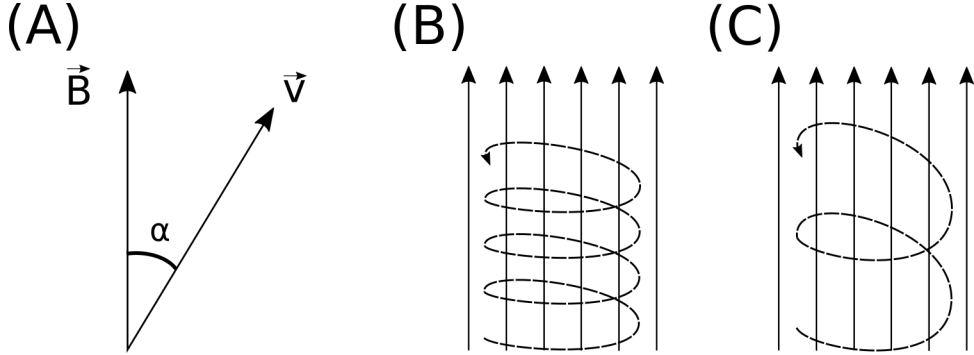


Figure 1.2: Charged particle motion in a uniform magnetic field \vec{B} . Panel (A) shows the geometry defining the pitch angle, α . Panel (B) and (C) show two helical electron trajectories with dashed lines assuming a large and small α (corresponding to a small and large parallel velocity $v_{||}$), respectively.

73 where m_n and m_s are the northern and southern mirror points, respectively. The
 74 bounce period can be estimated (e.g. Baumjohann and Treumann, 1997) to be

$$t_b \approx \frac{LR_e}{\sqrt{W/m}}(3.7 - 1.6 \sin \alpha(0)) \quad (1.10)$$

75 where W is the particle's kinetic energy, and L is the L -shell. The L -shell is the
 76 distance from the Earth's center to the location where a particular magnetic field
 77 line crosses the magnetic equator, in units of Earth radii, R_e . As with gyration, the
 78 particle will bounce between the mirror points as long as $\omega \ll \Omega_b$, where Ω_b is the
 79 bounce frequency.

80 At this stage it is instructional to introduce loss cone pitch angle, α_L .
 81 Conventionally, the loss cone pitch angle is defined as the pitch angle where a particle
 82 will mirror at ≈ 100 km altitude in the atmosphere. A charged particle gyrating at
 83 those altitudes will encounter and Coulomb scatter with the dense atmosphere and
 84 be lost. The 100 km altitude is only a convention and not a hard boundary, e.g. the
 85 peak in the 1 MeV electron ionization rate is at ≈ 60 km altitudes (Fang et al., 2010).

86 The slowest periodic motion experienced by charged particles in Earth's

87 magnetic field is azimuthal drift around the Earth. This drift primarily results from
 88 a combination of a radial gradient in \vec{B} and the curvature of the magnetic field. The
 89 radial gradient drift arises because Earth's magnetic field is stronger near the Earth.
 90 The particle's gyroradius shrinks as it gyrates towards Earth, and expands when it
 91 gyrates away from Earth. The overall effect is the particle gyro orbit does not close
 92 on itself causing eastward drift of negatively charged particles and westward drift
 93 of positively charged particles. The radial gradient drift is further enhanced by the
 94 centrifugal force that a particle experiences as it bounces along the curved field lines.
 95 The drift adiabatic invariant, J_3 is found by integrating Eq. 1.4 over the complete
 96 particle orbit around the Earth. The shape of this drift orbit is known as a drift shell,
 97 and can be visualized by rotating the trapped particle trajectory in Fig. 1.1 around
 98 the axis that connects the poles. For J_3 , the first term is negligible and the second
 99 term is the magnetic flux enclosed by the drift shell, Φ_m i.e. $J_3 \sim \Phi_m$ Add the J_3
 100 derivation.

101 To quantify the frequencies of the three periodic motions, Fig. 1.3 from Schulz
 102 and Lanzerotti (1974) shows contours of the gyration, bounce, and drift frequencies
 103 for electrons and protons in Earth's dipole magnetic field.

Up until now we have considered the three periodic motions due Earth's magnetic field in the absence of electric fields. If there is an electric field, \vec{E} , perpendicular to \vec{B} , a particle's center of gyration (averaged position of the particle over a gyration) will drift with a velocity perpendicular to both \vec{E} and \vec{B} . The drift velocity can be solved using Eq. 1.1 and is

$$\vec{v}_E = \frac{\vec{E} \times \vec{B}}{B^2}. \quad (1.11)$$

104 If there is a parallel magnetic field, $E_{||}$, then the particle is accelerated along the
 105 magnetic field line. An $E_{||}$ pointing away from the Earth will contribute to the mirror

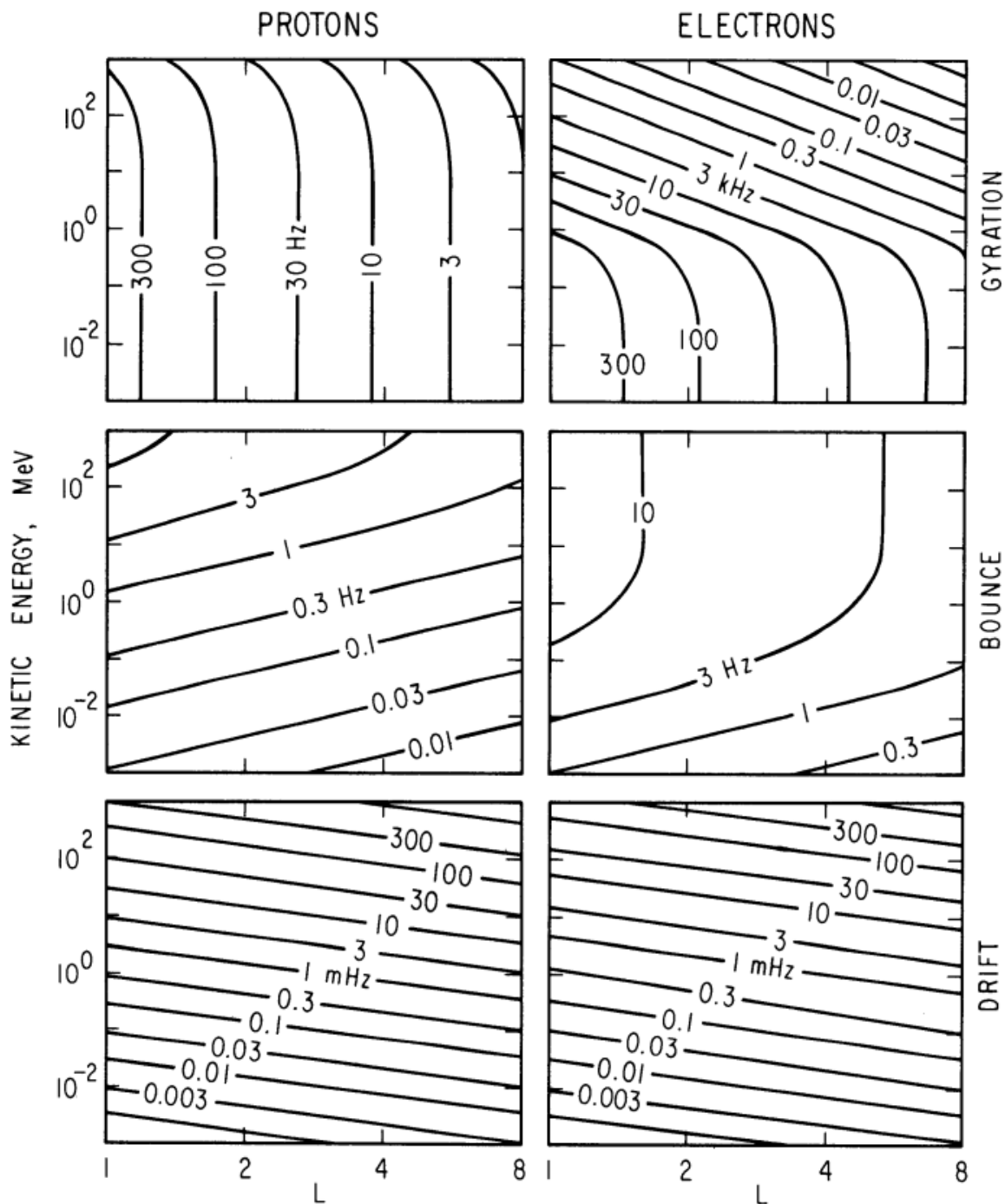


Figure 1.3: Contours of constant gyration, bounce, and drift frequencies for electrons and protons in a dipole field. Figure from Schulz and Lanzerotti (1974).

106 force and raise the particle's mirror point. On the contrary, an Earthward pointing
 107 $E_{||}$ will oppose the mirror force and lower the mirror point. If the Earthward $E_{||}$
 108 lowers the mirror point into the atmosphere, those particles will precipitate into the
 109 atmosphere. This is the mechanism that generates the aurora.

110 Particle Populations and Their Interractions in the Magnetosphere

111 Now that we have looked at the dynamics of single-particle motion in electric
 112 and magnetic fields, we will briefly tour the various macroscopic populations in the
 113 magnetosphere that are illustrated in Fig. 1.4.

114 The sun and its solar wind are ultimately the source of energy input into the
 115 magnetosphere. The solar wind at Earth's orbit is a plasma traveling at supersonic
 116 speeds with an embedded interplanetary magnetic field (IMF). When the solar wind
 117 encounters Earth's magnetic field, the plasma can not easily penetrate into the
 118 magnetosphere because the plasma is frozen-in on magnetic field lines. The plasma
 119 is frozen-in on magnetic field lines because plasma has a nearly infinite conductivity.
 120 Thus the plasma and its magnetic field drapes around the magnetosphere, forming a
 121 cavity in the solar wind that qualitatively has a shape as shown in Fig. 1.4. The solar
 122 wind is supersonic at 1 AU so a bow shock exists upstream of the magnetosphere
 123 which compresses and heats the solar wind. Downstream of the bow shock, the
 124 solar wind plasma flows around the magnetosphere inside the magnetosheath. The
 125 magnetopause is the surface where the solar wind ram and Earth's magnetic pressures
 126 balance. To first order, the magnetopause can be thought of as a boundary between
 127 the solar wind and Earth's magnetosphere. The shocked plasma then flows past the
 128 Earth where it shapes the magnetotail. In the magnetotail, the magnetopause exists
 129 where the solar wind magnetic pressure balances Earth's magnetic field pressure in
 130 the lobes. The magnetotail extends on the order of 100 R_E downstream of Earth,

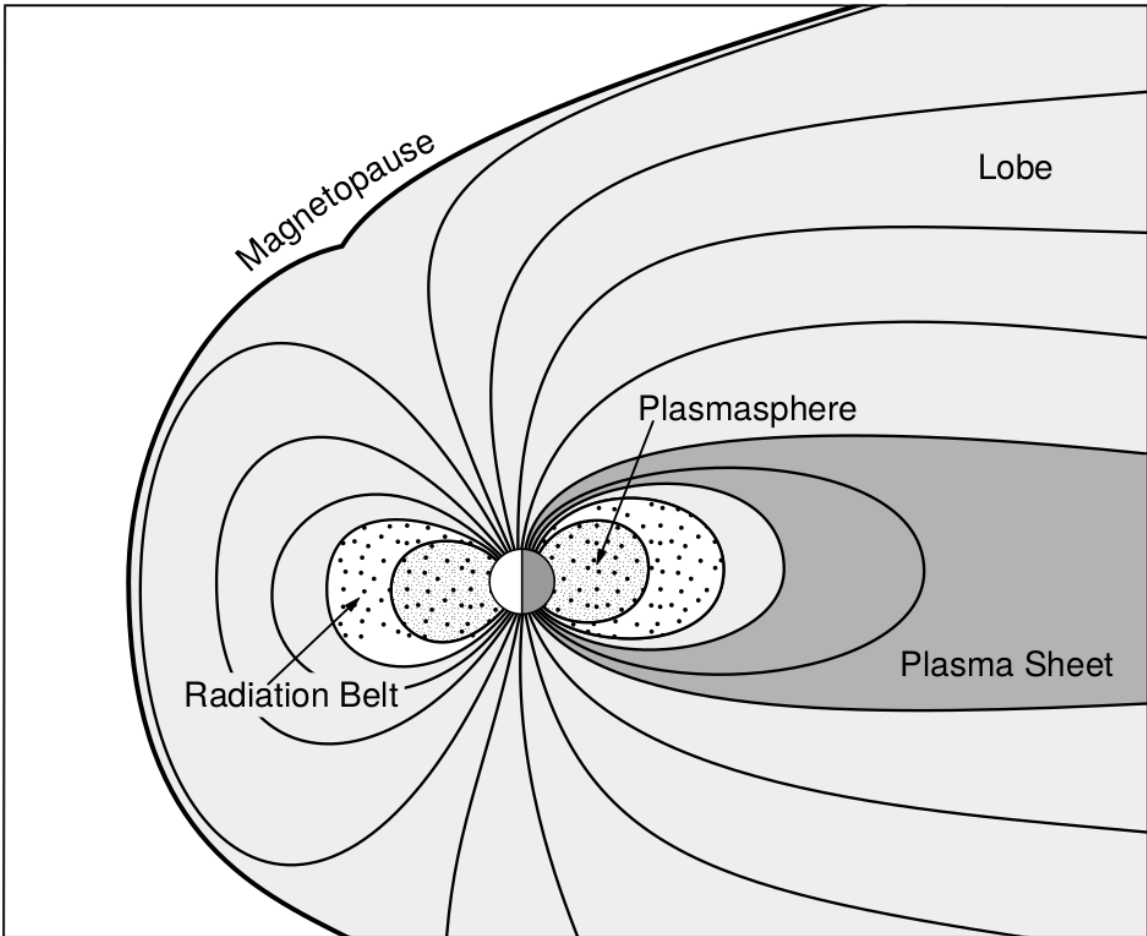


Figure 1.4: A few macroscopic structures in the magnetosphere. The magnetosphere boundary with the solar wind is the magnetopause. The magnetotail consists of two lobes that contain Earth's magnetic flux with the plasma sheet separating the two lobes. The inner magnetosphere contains the plasmasphere, the ring current, and the radiation belts which are co-located. Figure from Baumjohann and Treumann (1997).

and the tailward stretching of magnetic field lines creates a region where Earth's Earthward and anti-Earthward magnetic fields are in proximity. In this region, the curl of \vec{B} is non-zero, thus by Ampere's law there must be a current (called the plasma sheet) near the magnetic equator (e.g. Eastwood et al., 2015).

Populations in the Inner Magnetosphere

Closer to Earth, where the magnetic field is largely dipolar, are three plasma populations that comprise the inner magnetosphere: the plasmasphere, the ring current, and the radiation belts which are shown in Fig. 1.4. Before we describe these three particle populations in detail, we will introduce the coordinate system that most naturally describes the inner magnetosphere environment, and the electric fields that mostly effect low energy particles.

In this coordinate system the “radial” coordinate was defined in section 1 and is the L shell. The azimuthal coordinate is the magnetic local time (MLT). For an observer above Earth's north pole looking down, MLT is defined to be 0 (midnight) in the anti-sunward direction and increases in the counter-clockwise direction with 6 at dawn, 12 at noon (sunward direction), and 18 in dusk. The final coordinate is the magnetic latitude, λ , which is analogous to the latitude coordinate in the spherical coordinate system and is defined to be 0 at the magnetic equator. This coordinate system is shown in Fig. 1.5 and naturally describes the inner magnetosphere populations described below.

The low energy particle dynamics in the inner magnetosphere are organized by the co-rotation and the dawn-dusk (pointing from approximately 6 to 18 MLT) electric fields. The co-rotation electric field arises from Earth's rotation. Earth's magnetic field and the particles frozen on it rotate with the Earth so in the magnetosphere (non-rotating) reference frame the particles appear to $\vec{E} \times \vec{B}$ drift with Earth's

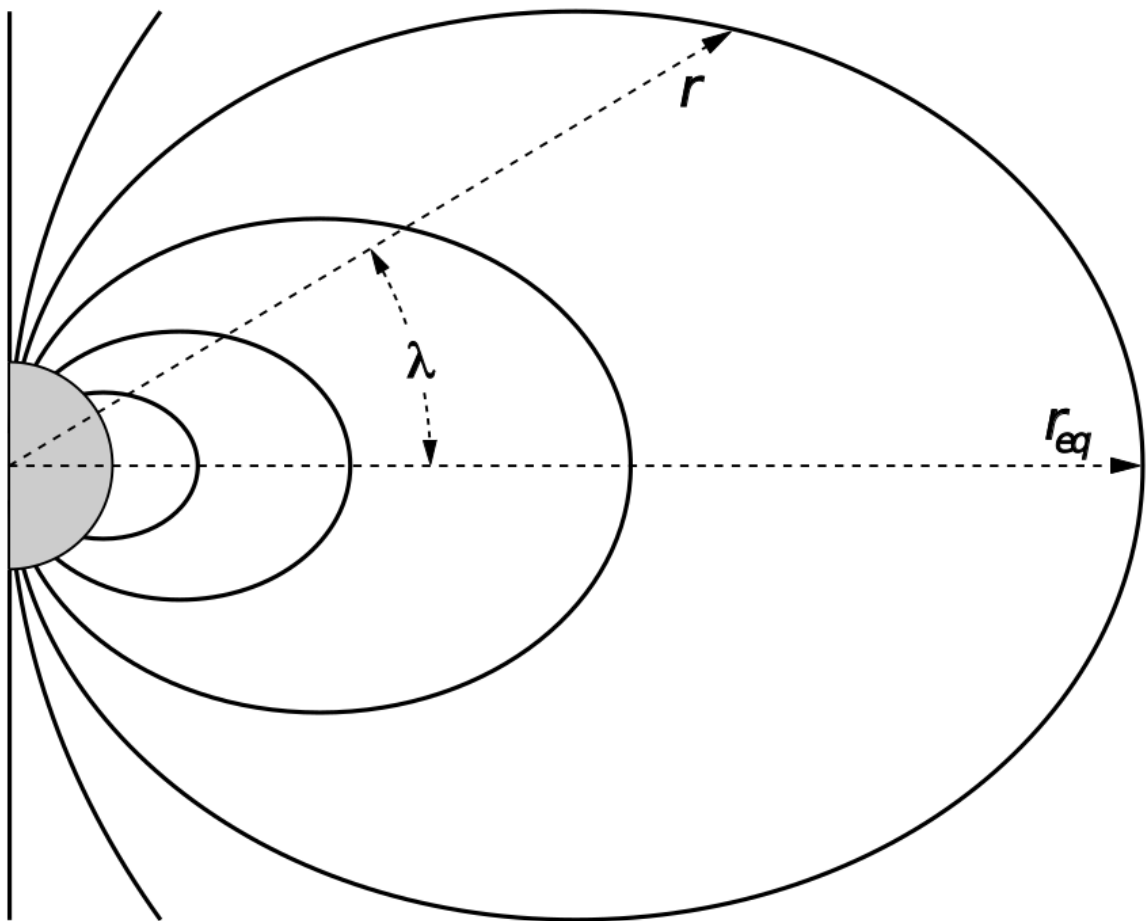


Figure 1.5: The dipole coordinate system. The magnetic latitude of \mathbf{r} is λ . The radial distance to a magnetic field line in the equatorial plane is typically given by $L = r_{eq}/R_e$. Figure from Baumjohann and Treumann (1997).

156 rotation. Make sure the E cross B drift is references correctly. Thus the co-rotation
 157 \vec{E} points towards Earth. The other electric field points from dawn to dusk is called
 158 the convection electric field and is due to the Earthward transport of particles from
 159 the magnetotail. In the magnetosphere reference frame this motion appears as an
 160 electric field pointing from dawn to dusk. The superposition of the co-rotation and
 161 and convection electric fields is a potential field shown in Fig. 1.6. The shaded
 162 area in Fig. 1.6 shows where low energy electrons execute closed orbits around Earth
 163 (i.e. particles are trapped), and outside this region the particles are not trapped. The
 164 dynamic topology of the shaded region in Fig. 1.6 is controlled by only the convection
 165 electric field which is dependent on the solar wind speed and the IMF. Due to $\vec{E} \times \vec{B}$
 166 drift, the lowest energy particles orbit along equipotential lines in the shaded region
 167 in Fig. 1.6 and make up the plasmasphere.

168 Plasmasphere The plasmasphere is a relatively dense ($n_e \sim 10^3/\text{cm}^3$) and cool
 169 ($\sim \text{eV}$) plasma. The plasmasphere typically extends to $L \sim 4$ and the spatial extent
 170 is highly dependent on the solar wind and magnetospheric conditions. The source
 171 of the plasmasphere is the ionosphere, a layer in Earth's upper atmosphere that
 172 contains a high concentration of electrons and ions. The main mechanisms that
 173 ionize the ionosphere are ultraviolet light from the sun and particle precipitation.
 174 The ultraviolet ionization by sunlight is strongly dependent on the time of day
 175 and latitude, while particle precipitation is highly dependent on magnetospheric
 176 conditions and mostly occurs at high latitudes.

177 The outer boundary of the plasmasphere is called the plasmapause which is
 178 typically identified by a steep radial gradient in plasma density from $\sim 10^3/\text{cm}^3$ to
 179 $\sim 1/\text{cm}^3$. It is important to know the location of the plasmapause since the plasma
 180 density strongly controls the efficiency of particle scattering by waves. For example,

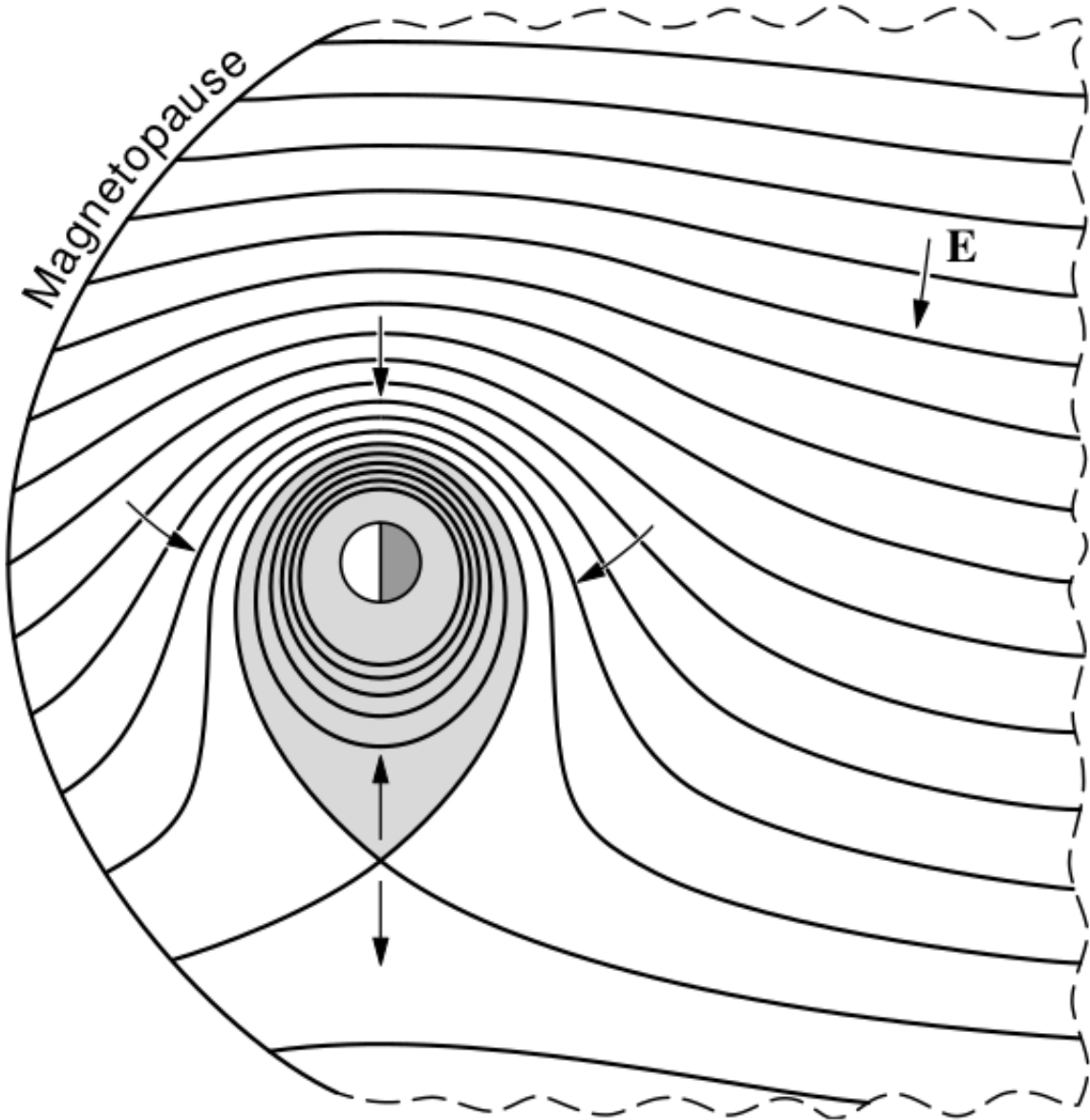


Figure 1.6: Equipotential lines and electric field arrows due to the superposition of the co-rotation and convection electric fields. Electrons in the shaded region execute closed orbits. Outside of the shaded regions the electrons are not trapped and will escape. The region separating the two regimes is called the Alfvén layer. Figure from Baumjohann and Treumann (1997).

181 electron scattering by chorus waves is more efficient when the ratio of the plasma and
 182 gyro frequency is low which is typically found in low plasma density regions outside
 183 of the plasmapause (e.g. Horne et al., 2003, 2005; O'Brien and Moldwin, 2003).

184 Ring Current A higher energy population is the ring current. This population
 185 consists of protons and electrons between tens and a few hundred keV that drift
 186 around the Earth. The orbits of higher energy particles are not as affected by the
 187 convection and co-rotation electric field, instead they drift around the Earth due to
 188 gradient and curvature drifts. Since the direction of the drift is dependent on charge,
 189 protons drift west around the Earth and electrons drift East. This effect creates a
 190 current around the Earth.

191 The ring current generates a magnetic field which decreases the magnetic field
 192 strength at the surface of the Earth and increases it outside of the ring current.
 193 The decrease of Earth's magnetic field strength is readily observed by a system of
 194 ground-based magnetometers and is merged into a Disturbance Storm Time (DST)
 195 index to quantify the global reduction in the magnetic field. An example of a DST
 196 index time series from the 2015 St. Patrick's Day storm, driven by a coronal mass
 197 ejection (CME), is shown in Fig. 1.7. A few notable features of the storm and the
 198 ring current are worth mentioning. At the start of the storm the ring current is
 199 sometimes depleted and DST increases slightly (termed the initial phase or sudden
 200 storm commencement) and is shown by the red horizontal bar in Fig. 1.7. During
 201 the main phase of the storm the ring current population is rapidly built up and DST
 202 rapidly decreases which is shown by the green bar in Fig. 1.7. After the storm passes,
 203 the ring current gradually decays toward its equilibrium state over a period of a few
 204 days and DST returns towards zero during the recovery phase which is shown by the
 205 blue bar in Fig. 1.7. The DST index, along with other geomagnetic indices, are used

206 by the space physics community to quantify the global state of the magnetosphere.

207 Radiation Belts The highest particle energy populations are in the Van Allen
208 radiation belts. These belts were discovered by Van Allen (1959) and Vernov and
209 Chudakov (1960) during the Cold War and are a pair of toroidally shaped populations
210 of trapped electrons and protons shown in Fig. 1.8. Their quiescent toroidal shape,
211 similar to the shape of the plasmasphere and ring current, is a result of Earth's dipole
212 magnetic field.

213 The inner radiation belt is extremely stable on time periods of years, extends
214 to $L \approx 2$, and mainly consists of protons with energies between MeV and GeV and
215 electrons with energies up to ≈ 1 MeV (Claudepierre et al., 2019). The source of
216 inner radiation belt protons is believed to be due to cosmic-ray albedo neutron decay
217 (e.g. Li et al., 2017) and inward radial diffusion for electrons (e.g. O'Brien et al.,
218 2016). The gap between the inner and outer radiation belt is called the slot, which is
219 believed to be due to hiss waves inside the plasmasphere (described below) scattering
220 particles into the atmosphere (e.g. Breneman et al., 2015; Lyons and Thorne, 1973).

221 The outer radiation belt is much more dynamic and consists of mainly electrons
222 of energies up to a few MeV. The outer belt's spatial extent is highly variable as
223 shown in Fig. 1.9, and is typically observed between L of 4 and 8. The source of
224 outer radiation belt electrons is widely believed to be injections of plasma from the
225 magnetotail that is then accelerated to high energies.

226 Due to the highly energetic and dynamic nature of the radiation belts, and
227 their impact on space exploration, the radiation belts have been studied for over half
228 century. Researchers have studied and attempted to predict the dynamics of radiation
229 belt particles, waves, and wave-particle interactions by considering various competing
230 particle acceleration and loss mechanisms which are described next.

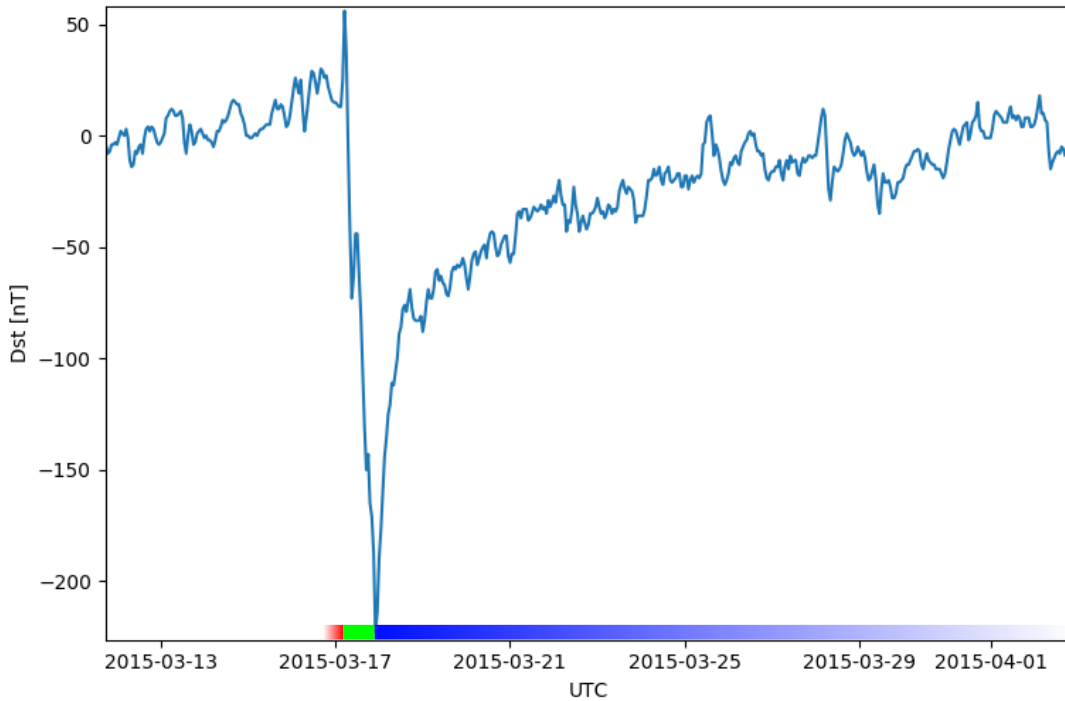


Figure 1.7: The DST index during the St. Patrick's Day 2015 storm. This storm was caused by a coronal mass ejection on March 15th, 2015. The storm phases are: initial phase, main phase, and recovery phase. The initial phase occurred when the Dst peaked at $+50$ nT on March 17th during which the ring current was eroded by the coronal mass ejection during the interval shown by the red bar shown at the bottom. Then the following rapid decrease to ≈ -200 nT was during the main phase where many injections from the magnetotail enhanced the ring current, which reduced Earth's magnetic field strength at the ground, and is shown with the green bar. Lastly, the recovery phase lasted from March 18th to approximately March 29th during which the ring current particles were lost and the ring current returned to its equilibrium state. The recovery phase is shown with the blue bar.

The Earth's Electron Radiation Belts

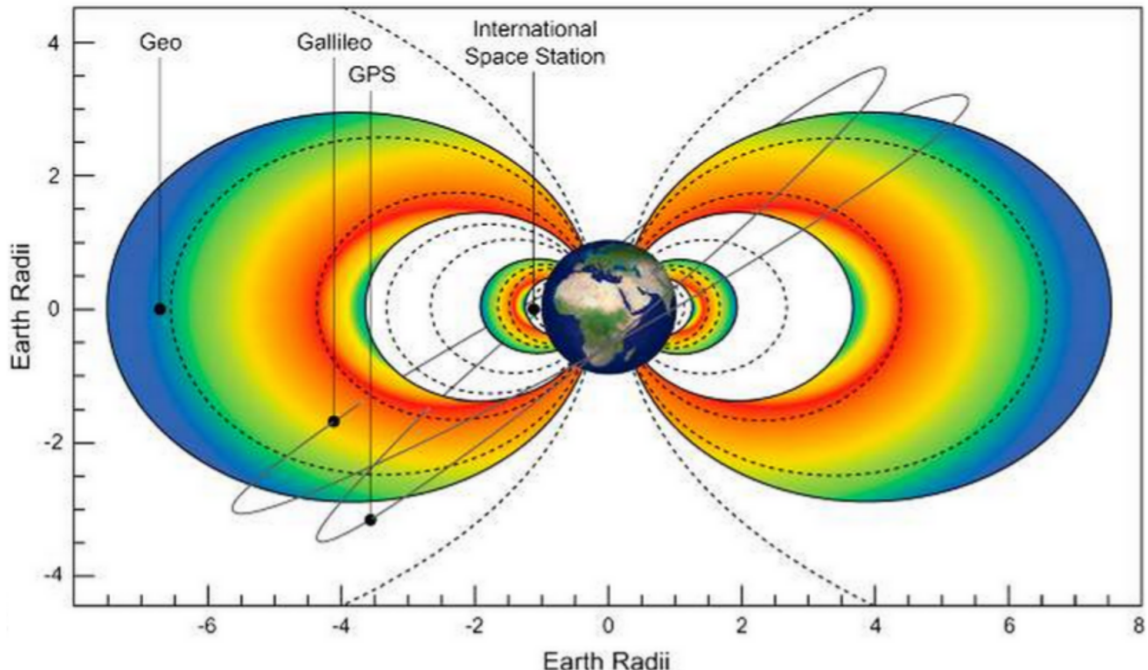


Figure 1.8: The two radiation belts with the locations of various satellites and orbits. Figure from (Horne et al., 2013).

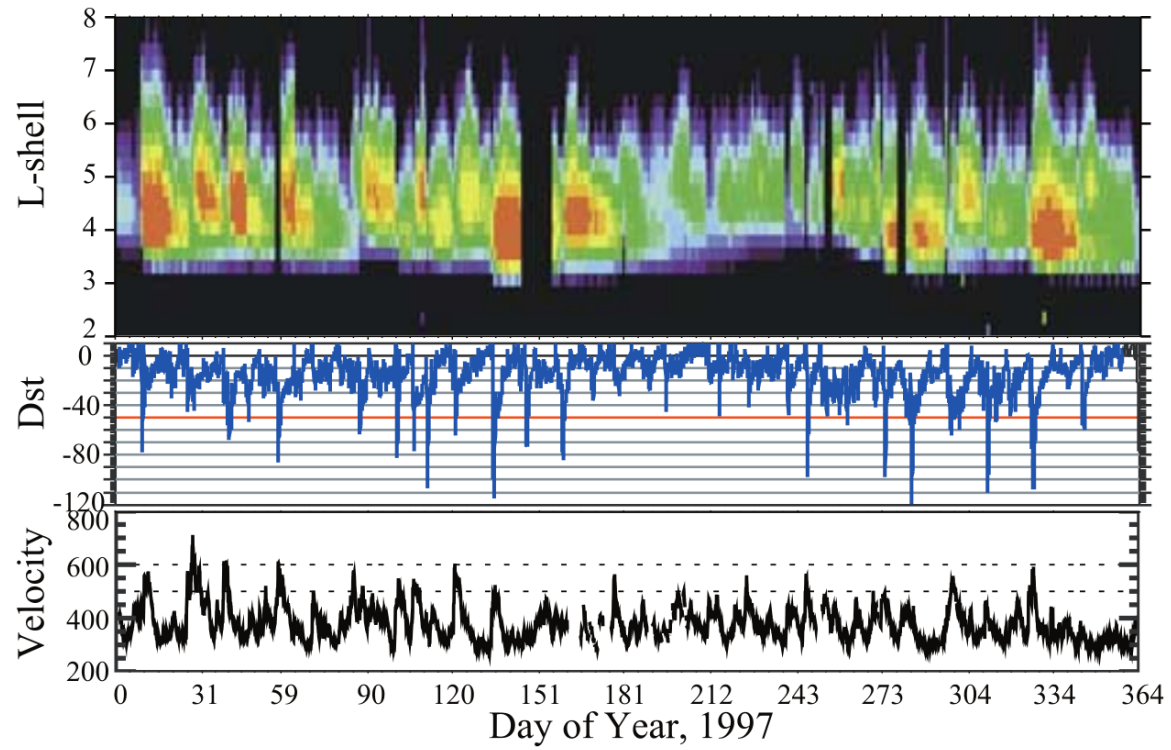


Figure 1.9: The dynamics of the outer radiation belt in 1997 from the POLAR satellite. Top panel shows the 1.2-2.4 MeV electron flux as a function of L and 1997 day of year. The middle panel shows the DST index, and bottom panel shows the solar wind velocity. Figure from (Reeves et al., 2003).

231

Radiation Belt Particle Sources and Sinks

232 In the magnetosphere there are a variety of mechanisms that add and remove
 233 particles. In the radiation belts, there is a complex interplay between these
 234 mechanisms that cause substantial changes to the radiation belt particle fluxes. An
 235 example of the complex radiation belt dynamics from 1997 is shown in the top panel
 236 in Fig. 1.9. This section will introduce a few mechanisms that contribute to the
 237 highly dynamic radiation belt fluxes including: adiabatic heating, wave-resonance
 238 heating, magnetopause shadowing, and wave-particle scattering.

239 Adiabatic Heating

240 One of the particle heating and transport mechanisms arises from the Earthward
 241 convection of particles. As shown in Eq. 1.5, the conservation of J_1 implies that the
 242 initial and final v_\perp depends on the change in the magnetic field magnitude. As a
 243 particle convects Earthward $B_f > B_i$ and thus v_\perp must also increase. The dipole
 244 magnetic field magnitude in micro Tesla (μT) can be written as

$$B(L, \lambda) = \frac{31.2 \text{ } \mu\text{T}}{L^3} \sqrt{1 + 3 \sin^2 \lambda} \quad (1.12)$$

245 The change in v_\perp^2 can be found by taking the ratio of $B(L, \lambda)$ at two different L shells

$$\frac{v_{\perp f}^2}{v_{\perp i}^2} = \left(\frac{L_i}{L_f} \right)^3 \quad (1.13)$$

246 thus the increase in $v_\perp \sim (L_i/L_f)^{3/2}$.

247 As the particle convects Earthward its $v_{||}$ also increases because the distance
 248 between the particle's mirror points decrease. Calculating the increase in $v_{||}$ is

²⁴⁹ somewhat difficult, but if J_2 is conserved the increase in v_{\parallel} is approximately

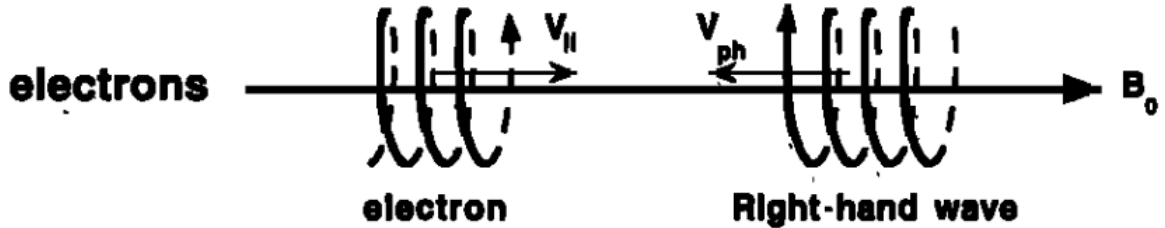
$$\frac{v_{\parallel f}^2}{v_{\parallel i}^2} = \left(\frac{L_i}{L_f} \right)^k \quad (1.14)$$

²⁵⁰ where k ranges from 2 for equatorial pitch angles, $\alpha_{eq} = 0^\circ$, to 2.5 for $\alpha_{eq} = 90^\circ$
²⁵¹ (Baumjohann and Treumann, 1997). Since the rate of adiabatic heating is greater in
²⁵² the perpendicular direction than heating in the parallel direction, an initially isotropic
²⁵³ particle distribution will become anisotropic during its convection. These isotropic
²⁵⁴ particles can then become unstable to wave growth and generate waves in order to
²⁵⁵ reach equilibrium.

²⁵⁶ Wave Resonance Heating

²⁵⁷ Another mechanism that heats particles is caused by particles resonating with
²⁵⁸ plasma waves. A few of the electromagnetic wave modes responsible for particle
²⁵⁹ acceleration (and scattering) relevant to radiation belt dynamics are hiss, whistler
²⁶⁰ mode chorus (chorus), and electromagnetic ion cyclotron (EMIC) waves. These waves
²⁶¹ are created by the loss cone instability that is driven by an anisotropy of electrons for
²⁶² chorus waves, and protons for EMIC waves. The level of anisotropy can be quantified
²⁶³ by the ratio of the perpendicular to parallel particle temperatures (T_{\perp}/T_{\parallel}). A particle
²⁶⁴ distribution is unstable when $T_{\perp}/T_{\parallel} > 1$. Since electrons gyrate in a right-handed
²⁶⁵ sense, the chorus waves also tend to be right hand circularly polarized (Tsurutani and
²⁶⁶ Lakhina, 1997). The same argument also applies to protons and left hand circularly
²⁶⁷ polarized EMIC waves.

²⁶⁸ These circularly polarized waves can resonate with electrons and/or protons
²⁶⁹ when their relative motion results in a static \vec{E} in the particle's reference frame. One
²⁷⁰ example of a resonance between a right hand circularly polarized wave and an electron
²⁷¹ is shown in Fig. 1.10. The electron's v_{\parallel} and the wave's parallel wave vector, k_{\parallel} , are in



$$\omega + k_{\parallel}v_{\parallel} = \Omega^-$$

Figure 1.10: The trajectories of an electron and a right-hand circularly polarized wave during a cyclotron resonance. The electron's v_{\parallel} and the wave's k_{\parallel} are in opposite directions such that the wave's frequency is Doppler shifted to an integer multiple of the electron cyclotron frequency. Figure from (Tsurutani and Lakhina, 1997).

²⁷² opposite directions such that the wave frequency, ω , is Doppler shifted to an integer
²⁷³ multiple of the Ω_e where the electron feels a static electric field and is accelerated or
²⁷⁴ decelerated. Quantitatively, this resonance condition is easier to understand with the
²⁷⁵ following toy model.

²⁷⁶ Assume a uniform magnetic field, $\vec{B} = B_0\hat{z}$, with a parallel propagating ($k = k\hat{z}$),
²⁷⁷ right-hand circularly polarized wave. The wave's electric field as a function of position
²⁷⁸ and time can be written as

$$\vec{E} = E_0(\cos(\omega t - kz)\hat{x} + \sin(\omega t - kz)\hat{y}). \quad (1.15)$$

The angular component of \vec{E} that will effect the particle's v_{\perp} is

$$E_{\theta} = \vec{E} \cdot \hat{\theta} = E_0 \cos(\omega t - kz + \theta). \quad (1.16)$$

²⁷⁹ Now assume that the electron is traveling in the $-\hat{z}$ direction with a velocity, $\vec{v} =$

²⁸⁰ $-v_0\hat{z}$, so its time dependent position along \hat{z} is

$$z(t) = -v_0 t \quad (1.17)$$

²⁸¹ and gyrophase is

$$\theta(t) = -\Omega t + \theta(0) \quad (1.18)$$

²⁸² where the first negative sign comes from the electron's negative charge. Now we put
²⁸³ this all together into Eq. 1.1 and find the force that the electron will experience is

$$m \frac{dv_\theta}{dt} = qE_\theta = qE_0 \sin((\omega + kv_0 - \Omega)t + \theta(0)). \quad (1.19)$$

²⁸⁴ This is a relatively complex expression, but when the time dependent component is
²⁸⁵ zero, i.e.

$$\omega + kv_0 - \Omega = 0, \quad (1.20)$$

²⁸⁶ the electron will feel a static electric field and be accelerated or decelerated depending
²⁸⁷ on θ_0 , the phase between the wave and the electron. The expression in Eq. 1.20 is
²⁸⁸ commonly referred to as the resonance condition and is more generally written as

$$\omega - k_{||}v_{||} = \frac{n\Omega_e}{\gamma} \quad (1.21)$$

²⁸⁹ where n is the resonance order, and γ is the relativistic correction (e.g. Millan and
²⁹⁰ Thorne, 2007). In the case of the cyclotron resonance ($n = 1$), the wave and cyclotron
²⁹¹ frequencies are approximately equal and thus J_1 is violated. Since J_1 is violated, J_2
²⁹² and J_3 are also violated since the conditions required to violate J_2 and J_3 are less
²⁹³ stringent than J_1 . It is important to remember that a particle will experience the

294 effects of many waves along its drift orbit. The typical MLT extent of a handful of
 295 waves that are capable of resonating with radiation belt electrons are shown in Fig.
 296 1.11.

297 Particle Losses

298 Now that we have seen two general mechanisms with which particles are
 299 accelerated in the magnetosphere, we will consider a few specific mechanisms that
 300 remove particles from the magnetosphere into the atmosphere or the solar wind.
 301 One mechanism that transports magnetosperic particles into the solar wind is
 302 magnetopause shadowing (e.g. Ukhorskiy et al., 2006). Magnetopause shadowing
 303 occurs when the ring current is strengthened and Earth's magnetic field strength is
 304 increased outside of the ring current. If the ring current increases slowly enough (such
 305 that J_3 is conserved), a particle drift shell will move outward to conserve J_3 . If the
 306 particle's drift shell expands past the magnetopause, the particle will be lost to the
 307 solar wind.

308 Another particle loss (and acceleration) mechanism is called radial diffusion and
 309 is driven by ultra low frequency (ULF) waves. Radial diffusion is the transport of
 310 particles from high to low phase space density, f . If the transport is radially inward,
 311 particles will appear to be accelerated. On the other hand, radially outward radial
 312 diffusion can transport particles through the magnetopause where they will be lost
 313 to the solar wind. Reeves et al. (2013) investigated the driver of particle acceleration
 314 during the October 2012 storm and observationally found that inward radial diffusion
 315 was not dominant, rather local acceleration via wave-resonance heating appeared to
 316 be the dominant acceleration mechanism.

317 The loss mechanism central to this dissertation is pitch angle and energy
 318 scattering of electrons by waves. Some of the waves that scatter electrons in energy

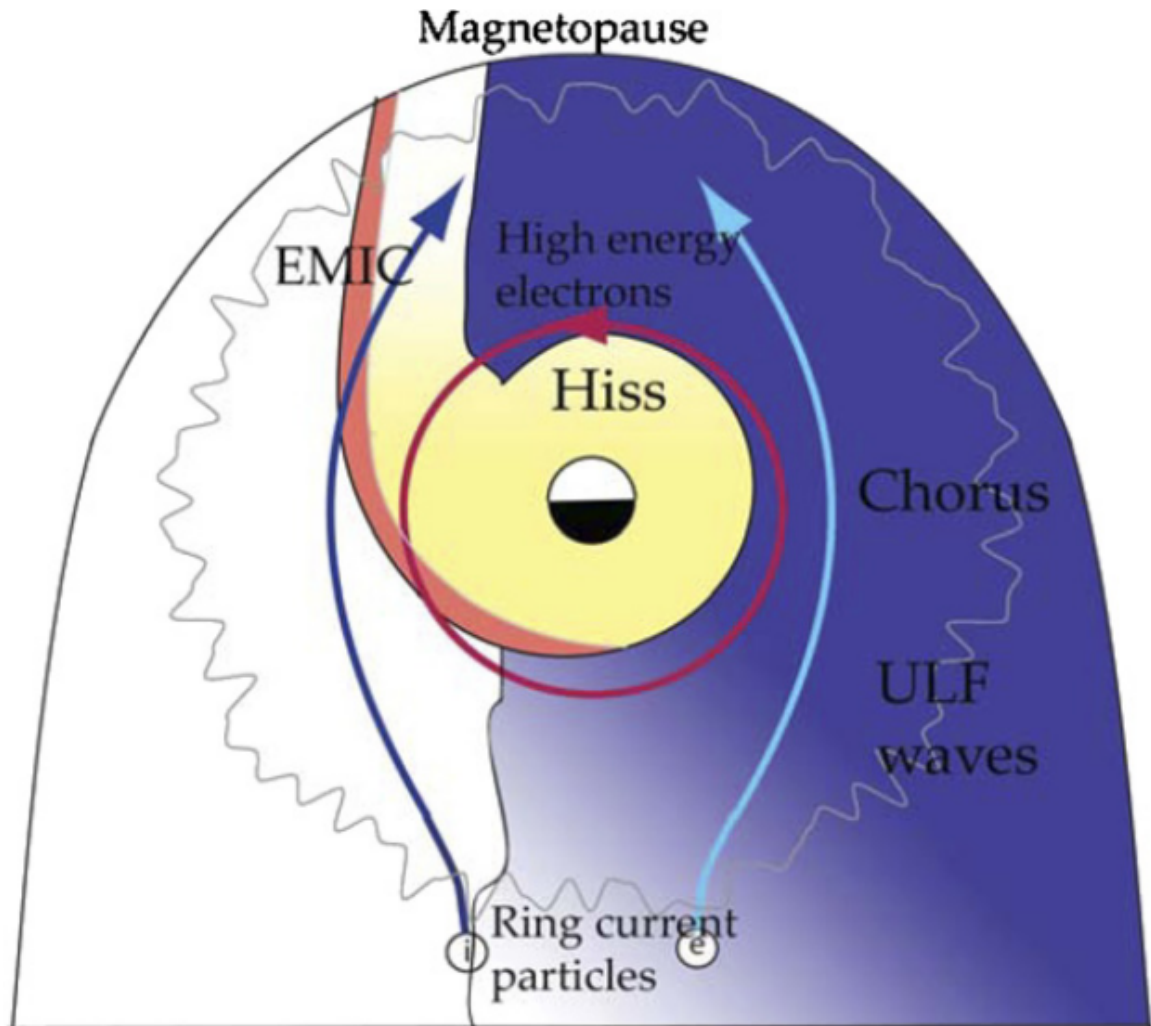


Figure 1.11: Various wave modes in the magnetosphere. Ultra low frequency waves occur through the magnetosphere. Chorus waves are typically observed in the 0-12 midnight-dawn region. EMIC waves are typically observed in the dusk MLT sector. Hiss waves are observed inside the plasmasphere. Figure from Millan and Thorne (2007).

and pitch angle in the inner magnetosphere are: plasmaspheric hiss (e.g. Breneman et al., 2015; O'Brien et al., 2014), EMIC waves (e.g. Capannolo et al., 2019; Hendry et al., 2017), and chorus waves (e.g. Breneman et al., 2017; Kasahara et al., 2018; Ozaki et al., 2019). These wave-particle interactions occur when the resonance condition in Eq. 1.21 is satisfied and the particle's energy and α is modified by the wave. More details regarding the theory of pitch angle and energy diffusion is given in Chapter ???. If the wave changes α towards zero and $\alpha < \alpha_L$, then the particle's mirror point dips below 100 km altitude where the particle can be lost from the magnetosphere. One manifestation of pitch angle scattering of particles into the loss cone are microbursts, a sub-second duration impulse of electrons.

329

Microbursts

Microbursts were first seen with high altitude balloons which measured bremsstrahlung X-rays emitted by microburst electrons impacting the atmosphere by Anderson and Milton (1964). In the following years, numerous balloon flights expanded our knowledge of non-relativistic (< 500 keV) microbursts by quantifying the microburst spatial extent, temporal width, occurrence frequency, extent in L and MLT, and their source. It is worth noting that relativistic microbursts have not yet been observed by high altitude balloons. The microburst source was initially believed to be either a local plasma instability or a propagating disturbance in the magnetosphere (Barcus et al., 1966; Brown et al., 1965; Parks, 1967; Trefall et al., 1966). Soon after, both non-relativistic and relativistic microburst electrons were directly observed in LEO with spacecraft including the Solar Anomalous and Magnetospheric Particle Explorer (SAMPEX) (e.g. Blake et al., 1996; Blum et al., 2015; Douma et al., 2019, 2017; Greeley et al., 2019; Lorentzen et al., 2001a,b; Nakamura et al., 1995, 2000; O'Brien et al., 2004, 2003), Montana State University's (MSU) Focused Investigation

344 of Relativistic Electron Bursts: Intensity, Range, and Dynamics II (FIREBIRD-II)
 345 (Anderson et al., 2017; Breneman et al., 2017; Crew et al., 2016; Klumpar et al.,
 346 2015; Spence et al., 2012), and Science Technologies Satellite (STSAT-I) (e.g. Lee
 347 et al., 2012, 2005). An example microburst time series is shown in Fig. 1.12 and was
 348 observed by the FIREBIRD-II CubeSats. The prominent features of the example
 349 microbursts in Fig. 1.12 are their sub-second duration, half order of magnitude
 350 increase in count rate above the falling background, and their 200-800 keV energy
 351 extent.

352 Microbursts are observed on magnetic field footprints that are connected to the
 353 outer radiation belt (approximately $4 < L < 8$). They are predominately observed in
 354 the 0-12 MLT sector with an elevated occurrence frequency during magnetospherically
 355 disturbed times as shown in Fig. 1.13 (e.g. Douma et al., 2017). O'Brien et al. (2003)
 356 used SAMPEX relativistic electron data and found that microbursts predominately
 357 occur during the main phase of storms, with a heightened occurrence rate during the
 358 recovery phase. Microburst occurrence rates are also higher during high solar wind
 359 velocity events e.g. from co-rotating interaction regions (Greeley et al., 2019; O'Brien
 360 et al., 2003).

361 The estimated impact of microbursts on the atmosphere and the radiation
 362 belts is significant. Relativistic microburst electrons impacting the atmosphere are
 363 ionized at < 100 km altitudes, with higher energy electrons penetrating closer to
 364 the surface. The resulting chemical reaction of microburst electrons impacting the
 365 atmosphere produces odd hydrogen HO_x and odd nitrogen NO_x molecules, which
 366 are partially responsible for destroying ozone (O_3). Seppälä et al. (2018) modeled
 367 a six hour relativistic microburst storm and found that the mesospheric ozone was
 368 reduced by 7 – 12% in the summer months and 12 – 20% in the winter months, so
 369 microbursts may have a non-negligible contribution to the dynamics of atmospheric

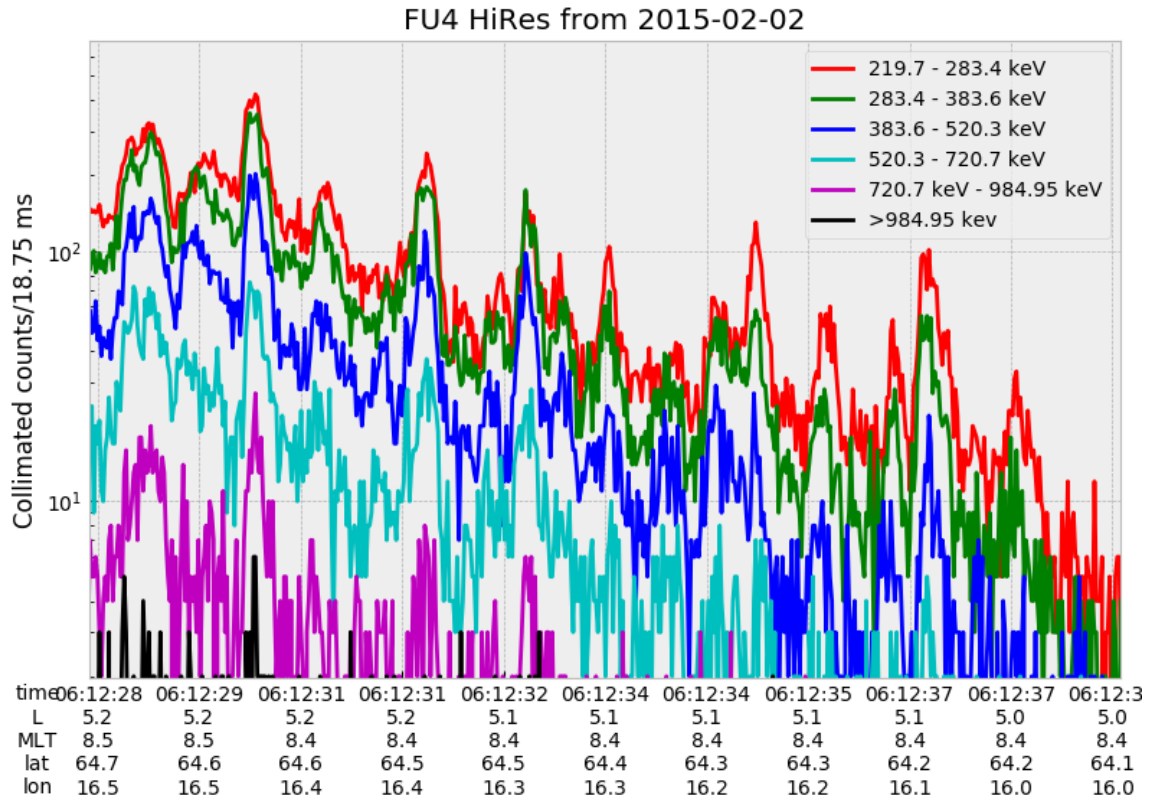


Figure 1.12: An example train of microbursts observed by FIREBIRD-II unit 4 on February 2nd, 2015. The colored curves show the differential energy channel count rates in five channels from ≈ 200 keV to 1 MeV and a sixth integral energy channel with a 1 MeV threshold. The x-axis labels show auxiliary information such as time of observation and the spacecraft position in L, MLT, latitude and longitude coordinates.

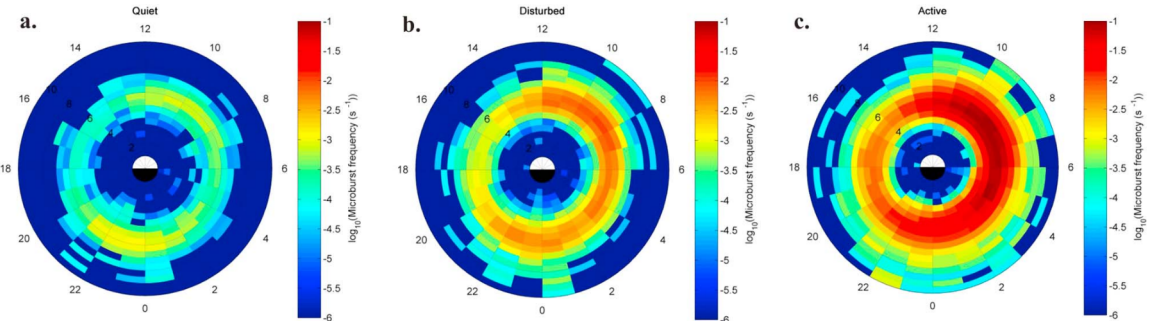


Figure 1.13: Distribution of > 1 MeV microburst occurrence rates as a function of L and MLT. The three panels show the microburst occurrence rate dependence on geomagnetic activity, parameterized by the auroral electrojet (AE) index for (a) $\text{AE} < 100$ nT, (b) $100 < \text{AE} < 300$ nT and (c) $\text{AE} > 300$ nT. Figure from Douma et al. (2017).

ozone. Furthermore, microbursts have also been estimated to have a significant impact on the outer radiation belt electron population. The loss of all radiation belt electrons due to microbursts have been estimated to be on the order of a day (Breneman et al., 2017; Douma et al., 2019; Lorentzen et al., 2001b; O'Brien et al., 2004; Thorne et al., 2005).

The wave-particle interactions responsible for generating microbursts are also believed to accelerate electrons in the radiation belts. As mentioned earlier, when an electron is in resonance with a wave, energy is exchanged with the wave and the electron is either accelerated or decelerated. The signature of wave-particle acceleration been observed for radiation belt electrons (e.g. Horne et al., 2005; Meredith et al., 2002; Reeves et al., 2013), and O'Brien et al. (2003) presented evidence that enhancements in chorus waves, microbursts, and radiation belt electrons are related. To explain their observations, O'Brien et al. (2003) proposed that microburst precipitation is a side effect of electron acceleration due to chorus waves.

The widely used theoretical framework to model the wave-particle interactions responsible for accelerating electrons and scattering microbursts is quasi-linear

386 diffusion (e.g. Horne et al., 2005; Meredith et al., 2002; Summers, 2005; Summers
 387 et al., 1998; Thorne et al., 2005; Walker, 1993). This framework is explained in
 388 Chapter ??, and applied to an observation of a microburst in the heart of the
 389 radiation belt. Qualitatively, when a particle is resonant with a wave it can either
 390 be transported in pitch angle towards the loss cone and lose energy to the wave, or
 391 transported away from the loss cone and gain energy from the wave.

392 As previously mentioned, the range of observed microburst energies range from a
 393 few tens of keV (e.g Datta et al., 1997; Parks, 1967) to greater than 1 MeV (e.g. Blake
 394 et al., 1996; Greeley et al., 2019). The microburst electron flux (J) falls off in energy,
 395 and the microburst energy spectra is typically well fit to a decaying exponential

$$J(E) = J_0 e^{-E/E_0} \quad (1.22)$$

396 where J_0 is the flux at 0 keV (unphysical free parameter) and E_0 quantifies the
 397 efficiency of the scattering mechanism in energy (e.g. Datta et al., 1997; Lee et al.,
 398 2005; Parks, 1967). A small E_0 suggests that mostly low energy particles are scattered.
 399 In contrast a high E_0 suggests that the scattering mechanism scatters low and high
 400 energy electrons. Reality is a bit more messy and a high E_0 may be a signature of a
 401 scattering mechanism that is most efficient at scattering high energy electrons, with a
 402 relatively minor efficiency to scatter low energy electrons. Since there are many more
 403 low energy electrons available to scatter, there may be relatively more low energy
 404 electrons scattered.

405 The short microburst duration, as observed by a single LEO satellite in a highly
 406 inclined orbit (motion is mostly latitudinal), has an ambiguity when interpreting what
 407 is a microburst. The two possible realities are: a microburst is very narrow in latitude
 408 and persistent, or spatially large and transient. There are a few ways to distinguish

409 between the two possible realities, and each one has a unique set of advantages.

410 A high altitude balloon essentially provides a stationary view of the precipitating
 411 particles under the radiation belt footprints. An intense transient microburst can be
 412 unambiguously identified above the slowly varying background. On the other hand,
 413 if the microburst precipitation is stationary, there will be too little contrast between
 414 the microburst and the background fluxes to be found.

415 Multi-spacecraft missions provide an alternate solution that can determine if
 416 a microburst is a spatial or a transient phenomena. As is illustrated in Fig. 1.14,
 417 a transient microburst can be recognized if both spacecraft simultaneously observe
 418 it. The size of the microburst footprint must then be larger than the spacecraft
 419 separation. On the contrary, if two spacecraft observe a microburst-like feature at
 420 the same location but at different times, then the feature is stationary and may be a
 421 curtain (Blake and O'Brien, 2016). Both balloon and multi-spacecraft observational
 422 methods have a unique set of strengths. This dissertation takes the multi-spacecraft
 423 approach to identify and study microbursts.

424

Scope of Research

425 This dissertation furthers our understanding of the microburst scattering
 426 mechanism by presenting observational evidence of microburst scattering directly,
 427 and measuring microburst sizes and comparing them to the size of chorus waves.
 428 Chapter ?? describes a microburst scattering event observed by NASA's Van Allen
 429 Probes. For this event, particle and wave measurements were analyzed and modeled
 430 in the theoretical framework of pitch angle and energy diffusion. The following two
 431 chapters present studies of microburst sizes in comparison to chorus waves. Chapter
 432 ?? describes a bouncing packet microburst observation made by the FIREBIRD-II
 433 mission where the microburst's lower bound longitudinal and latitudinal sizes were

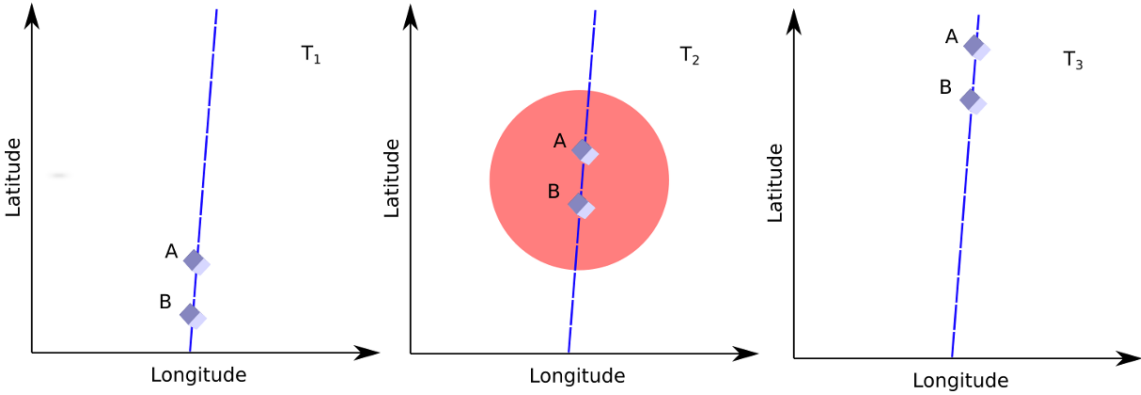


Figure 1.14: Three snapshots of a temporal microburst observed simultaneously by a pair of polar-orbiting spacecraft. The spacecraft are identified by labels "A" and "B" and are traveling upwards on the blue dashed orbital track. At T_1 the spacecraft are traveling upwards and no microburst is observed. Then at T_2 both spacecraft simultaneously observe a microburst shown by the red circle. In the last snapshot, T_3 , the microburst has precipitated and no longer observed by the spacecraft.

⁴³⁴ estimated. Chapter ?? expands the case study from Chapter ?? to a statistical study
⁴³⁵ of microburst sizes using The Aerospace Corporation's AeroCube-6 (AC6) CubeSats.
⁴³⁶ In this study, a Monte Carlo and analytic microburst size models were developed
⁴³⁷ to account for the compounding statistical effects of random microburst sizes and
⁴³⁸ locations. Lastly, Chapter ?? will summarize this work and make concluding remarks
⁴³⁹ regarding outstanding questions in microburst physics.

- 441 Anderson, B., Shekhar, S., Millan, R., Crew, A., Spence, H., Klumpar, D., Blake, J.,
 442 O'Brien, T., and Turner, D. (2017). Spatial scale and duration of one microburst
 443 region on 13 August 2015. *Journal of Geophysical Research: Space Physics*.
- 444 Anderson, K. A. and Milton, D. W. (1964). Balloon observations of X rays in the
 445 auroral zone: 3. High time resolution studies. *Journal of Geophysical Research*,
 446 69(21):4457–4479.
- 447 Barcus, J., Brown, R., and Rosenberg, T. (1966). Spatial and temporal character of
 448 fast variations in auroral-zone x rays. *Journal of Geophysical Research*, 71(1):125–
 449 141.
- 450 Baumjohann, W. and Treumann, R. A. (1997). *Basic space plasma physics*. World
 451 Scientific.
- 452 Blake, J.,Looper, M., Baker, D., Nakamura, R., Klecker, B., and Hovestadt, D.
 453 (1996). New high temporal and spatial resolution measurements by sampex of the
 454 precipitation of relativistic electrons. *Advances in Space Research*, 18(8):171 – 186.
- 455 Blake, J. B. and O'Brien, T. P. (2016). Observations of small-scale latitudinal
 456 structure in energetic electron precipitation. *Journal of Geophysical Research: Space
 457 Physics*, 121(4):3031–3035. 2015JA021815.
- 458 Blum, L., Li, X., and Denton, M. (2015). Rapid MeV electron precipitation as
 459 observed by SAMPEX/HILT during high-speed stream-driven storms. *Journal of
 460 Geophysical Research: Space Physics*, 120(5):3783–3794. 2014JA020633.
- 461 Breneman, A., Crew, A., Sample, J., Klumpar, D., Johnson, A., Agapitov, O.,
 462 Shumko, M., Turner, D., Santolik, O., Wygant, J., et al. (2017). Observations
 463 directly linking relativistic electron microbursts to whistler mode chorus: Van allen
 464 probes and FIREBIRD II. *Geophysical Research Letters*.
- 465 Breneman, A. W., Halford, A., Millan, R., McCarthy, M., Fennell, J., Sample, J.,
 466 Woodger, L., Hospodarsky, G., Wygant, J. R., Cattell, C. A., et al. (2015). Global-
 467 scale coherence modulation of radiation-belt electron loss from plasmaspheric hiss.
 468 *Nature*, 523(7559):193.
- 469 Brown, R., Barcus, J., and Parsons, N. (1965). Balloon observations of auroral zone
 470 x rays in conjugate regions. 2. microbursts and pulsations. *Journal of Geophysical
 471 Research (U.S.)*.
- 472 Capannolo, L., Li, W., Ma, Q., Shen, X.-C., Zhang, X.-J., Redmon, R., Rodriguez,
 473 J., Engebretson, M., Kletzing, C., Kurth, W., et al. (2019). Energetic electron
 474 precipitation: multi-event analysis of its spatial extent during emic wave activity.
 475 *Journal of Geophysical Research: Space Physics*.

- 476 Claudepierre, S., O'Brien, T.,Looper, M., Blake, J., Fennell, J., Roeder, J.,
 477 Clemmons, J., Mazur, J., Turner, D., Reeves, G., et al. (2019). A revised look
 478 at relativistic electrons in the earth's inner radiation zone and slot region. *Journal
 479 of Geophysical Research: Space Physics*, 124(2):934–951.
- 480 Crew, A. B., Spence, H. E., Blake, J. B., Klumpar, D. M., Larsen, B. A., O'Brien,
 481 T. P., Driscoll, S., Handley, M., Legere, J., Longworth, S., Mashburn, K.,
 482 Mosleh, E., Ryhajlo, N., Smith, S., Springer, L., and Widholm, M. (2016). First
 483 multipoint in situ observations of electron microbursts: Initial results from the
 484 NSF FIREBIRD II mission. *Journal of Geophysical Research: Space Physics*,
 485 121(6):5272–5283. 2016JA022485.
- 486 Datta, S., Skoug, R., McCarthy, M., and Parks, G. (1997). Modeling of microburst
 487 electron precipitation using pitch angle diffusion theory. *Journal of Geophysical
 488 Research: Space Physics*, 102(A8):17325–17333.
- 489 Douma, E., Rodger, C., Blum, L., O'Brien, T., Clilverd, M., and Blake, J. (2019).
 490 Characteristics of relativistic microburst intensity from sampex observations.
 491 *Journal of Geophysical Research: Space Physics*.
- 492 Douma, E., Rodger, C. J., Blum, L. W., and Clilverd, M. A. (2017). Occurrence
 493 characteristics of relativistic electron microbursts from SAMPEX observations.
 494 *Journal of Geophysical Research: Space Physics*, 122(8):8096–8107. 2017JA024067.
- 495 Eastwood, J., Hietala, H., Toth, G., Phan, T., and Fujimoto, M. (2015). What
 496 controls the structure and dynamics of earths magnetosphere? *Space Science
 497 Reviews*, 188(1-4):251–286.
- 498 Fang, X., Randall, C. E., Lummerzheim, D., Wang, W., Lu, G., Solomon, S. C., and
 499 Frahm, R. A. (2010). Parameterization of monoenergetic electron impact ionization.
 500 *Geophysical Research Letters*, 37(22).
- 501 Greeley, A., Kanekal, S., Baker, D., Klecker, B., and Schiller, Q. (2019). Quantifying
 502 the contribution of microbursts to global electron loss in the radiation belts. *Journal
 503 of Geophysical Research: Space Physics*.
- 504 Hendry, A. T., Rodger, C. J., and Clilverd, M. A. (2017). Evidence of sub-mev
 505 emic-driven electron precipitation. *Geophysical Research Letters*, 44(3):1210–1218.
- 506 Horne, R., Glauert, S., Meredith, N., Boscher, D., Maget, V., Heynderickx, D., and
 507 Pitchford, D. (2013). Space weather impacts on satellites and forecasting the earth's
 508 electron radiation belts with spacecast. *Space Weather*, 11(4):169–186.
- 509 Horne, R., Glauert, S., and Thorne, R. (2003). Resonant diffusion of radiation belt
 510 electrons by whistler-mode chorus. *Geophysical research letters*, 30(9).

- 511 Horne, R. B., Thorne, R. M., Shprits, Y. Y., Meredith, N. P., Glauert, S. A., Smith,
 512 A. J., Kanekal, S. G., Baker, D. N., Engebretson, M. J., Posch, J. L., et al.
 513 (2005). Wave acceleration of electrons in the van allen radiation belts. *Nature*,
 514 437(7056):227.
- 515 Kasahara, S., Miyoshi, Y., Yokota, S., Mitani, T., Kasahara, Y., Matsuda, S.,
 516 Kumamoto, A., Matsuoka, A., Kazama, Y., Frey, H., et al. (2018). Pulsating
 517 aurora from electron scattering by chorus waves. *Nature*, 554(7692):337.
- 518 Klumper, D., Springer, L., Mosleh, E., Mashburn, K., Berardinelli, S., Gunderson,
 519 A., Handly, M., Ryhajlo, N., Spence, H., Smith, S., Legere, J., Widholm, M.,
 520 Longworth, S., Crew, A., Larsen, B., Blake, J., and Walmsley, N. (2015). Flight
 521 system technologies enabling the twin-cubesat firebird-ii scientific mission.
- 522 Lee, J. J., Parks, G. K., Lee, E., Tsurutani, B. T., Hwang, J., Cho, K. S., Kim, K.-H.,
 523 Park, Y. D., Min, K. W., and McCarthy, M. P. (2012). Anisotropic pitch angle
 524 distribution of 100 keV microburst electrons in the loss cone: measurements from
 525 STSAT-1. *Annales Geophysicae*, 30(11):1567–1573.
- 526 Lee, J.-J., Parks, G. K., Min, K. W., Kim, H. J., Park, J., Hwang, J., McCarthy,
 527 M. P., Lee, E., Ryu, K. S., Lim, J. T., Sim, E. S., Lee, H. W., Kang, K. I., and
 528 Park, H. Y. (2005). Energy spectra of 170–360 keV electron microbursts measured
 529 by the korean STSAT-1. *Geophysical Research Letters*, 32(13). L13106.
- 530 Li, X., Selesnick, R., Schiller, Q., Zhang, K., Zhao, H., Baker, D. N., and Temerin,
 531 M. A. (2017). Measurement of electrons from albedo neutron decay and neutron
 532 density in near-earth space. *Nature*, 552(7685):382.
- 533 Lorentzen, K. R., Blake, J. B., Inan, U. S., and Bortnik, J. (2001a). Observations
 534 of relativistic electron microbursts in association with VLF chorus. *Journal of
 535 Geophysical Research: Space Physics*, 106(A4):6017–6027.
- 536 Lorentzen, K. R., Looper, M. D., and Blake, J. B. (2001b). Relativistic electron
 537 microbursts during the GEM storms. *Geophysical Research Letters*, 28(13):2573–
 538 2576.
- 539 Lyons, L. R. and Thorne, R. M. (1973). Equilibrium structure of radiation belt
 540 electrons. *Journal of Geophysical Research*, 78(13):2142–2149.
- 541 Meredith, N., Horne, R., Summers, D., Thorne, R., Iles, R., Heynderickx, D., and
 542 Anderson, R. (2002). Evidence for acceleration of outer zone electrons to relativistic
 543 energies by whistler mode chorus. In *Annales Geophysicae*, volume 20, pages 967–
 544 979.
- 545 Millan, R. and Thorne, R. (2007). Review of radiation belt relativistic electron losses.
 546 *Journal of Atmospheric and Solar-Terrestrial Physics*, 69(3):362 – 377.

- 547 Nakamura, R., Baker, D. N., Blake, J. B., Kanekal, S., Klecker, B., and Hovestadt,
 548 D. (1995). Relativistic electron precipitation enhancements near the outer edge of
 549 the radiation belt. *Geophysical Research Letters*, 22(9):1129–1132.
- 550 Nakamura, R., Isowa, M., Kamide, Y., Baker, D., Blake, J., and Looper, M. (2000).
 551 Observations of relativistic electron microbursts in association with VLF chorus.
 552 *J. Geophys. Res.*, 105:15875–15885.
- 553 O'Brien, T., Claudepierre, S., Blake, J., Fennell, J. F., Clemons, J., Roeder, J.,
 554 Spence, H. E., Reeves, G., and Baker, D. (2014). An empirically observed pitch-
 555 angle diffusion eigenmode in the earth's electron belt near $l^*= 5.0$. *Geophysical*
 556 *Research Letters*, 41(2):251–258.
- 557 O'Brien, T., Claudepierre, S., Guild, T., Fennell, J., Turner, D., Blake, J., Clemons,
 558 J., and Roeder, J. (2016). Inner zone and slot electron radial diffusion revisited.
 559 *Geophysical Research Letters*, 43(14):7301–7310.
- 560 O'Brien, T. and Moldwin, M. (2003). Empirical plasmapause models from magnetic
 561 indices. *Geophysical Research Letters*, 30(4).
- 562 O'Brien, T. P., Looper, M. D., and Blake, J. B. (2004). Quantification of relativistic
 563 electron microburst losses during the GEM storms. *Geophysical Research Letters*,
 564 31(4). L04802.
- 565 O'Brien, T. P., Lorentzen, K. R., Mann, I. R., Meredith, N. P., Blake, J. B., Fennell,
 566 J. F., Looper, M. D., Milling, D. K., and Anderson, R. R. (2003). Energization of
 567 relativistic electrons in the presence of ULF power and MeV microbursts: Evidence
 568 for dual ULF and VLF acceleration. *Journal of Geophysical Research: Space*
 569 *Physics*, 108(A8).
- 570 Ozaki, M., Miyoshi, Y., Shiokawa, K., Hosokawa, K., Oyama, S.-i., Kataoka, R.,
 571 Ebihara, Y., Ogawa, Y., Kasahara, Y., Yagitani, S., et al. (2019). Visualization of
 572 rapid electron precipitation via chorus element wave–particle interactions. *Nature*
 573 *communications*, 10(1):257.
- 574 Parks, G. K. (1967). Spatial characteristics of auroral-zone X-ray microbursts. *Journal*
 575 *of Geophysical Research*, 72(1):215–226.
- 576 Reeves, G., Spence, H. E., Henderson, M., Morley, S., Friedel, R., Funsten, H., Baker,
 577 D., Kanekal, S., Blake, J., Fennell, J., et al. (2013). Electron acceleration in the
 578 heart of the van allen radiation belts. *Science*, 341(6149):991–994.
- 579 Reeves, G. D., McAdams, K. L., Friedel, R. H. W., and O'Brien, T. P. (2003). Ac-
 580 celeration and loss of relativistic electrons during geomagnetic storms. *Geophysical*
 581 *Research Letters*, 30(10):n/a–n/a. 1529.

- 582 Schulz, M. and Lanzerotti, L. J. (1974). *Particle Diffusion in the Radiation Belts*.
 583 Springer.
- 584 Seppälä, A., Douma, E., Rodger, C., Verronen, P., Clilverd, M. A., and Bortnik, J.
 585 (2018). Relativistic electron microburst events: Modeling the atmospheric impact.
 586 *Geophysical Research Letters*, 45(2):1141–1147.
- 587 Spence, H. E., Blake, J. B., Crew, A. B., Driscoll, S., Klumpar, D. M., Larsen,
 588 B. A., Legere, J., Longworth, S., Mosleh, E., O'Brien, T. P., Smith, S., Springer,
 589 L., and Widholm, M. (2012). Focusing on size and energy dependence of electron
 590 microbursts from the van allen radiation belts. *Space Weather*, 10(11).
- 591 Summers, D. (2005). Quasi-linear diffusion coefficients for field-aligned electro-
 592 magnetic waves with applications to the magnetosphere. *Journal of Geophysical
 593 Research: Space Physics*, 110(A8):n/a–n/a. A08213.
- 594 Summers, D., Thorne, R. M., and Xiao, F. (1998). Relativistic theory of wave-particle
 595 resonant diffusion with application to electron acceleration in the magnetosphere.
 596 *Journal of Geophysical Research: Space Physics*, 103(A9):20487–20500.
- 597 Thorne, R. M., O'Brien, T. P., Shprits, Y. Y., Summers, D., and Horne, R. B. (2005).
 598 Timescale for MeV electron microburst loss during geomagnetic storms. *Journal
 599 of Geophysical Research: Space Physics*, 110(A9). A09202.
- 600 Trefall, H., Bjordal, J., Ullaland, S., and Stadsnes, J. (1966). On the extension of
 601 auroral-zone x-ray microbursts. *Journal of Atmospheric and Terrestrial Physics*,
 602 28(2):225–233.
- 603 Tsurutani, B. T. and Lakhina, G. S. (1997). Some basic concepts of wave-particle
 604 interactions in collisionless plasmas. *Reviews of Geophysics*, 35(4):491–501.
- 605 Ukhorskiy, A. Y., Anderson, B. J., Brandt, P. C., and Tsyganenko, N. A. (2006).
 606 Storm time evolution of the outer radiation belt: Transport and losses. *Journal of
 607 Geophysical Research: Space Physics*, 111(A11):n/a–n/a. A11S03.
- 608 Van Allen, J. A. (1959). The geomagnetically trapped corpuscular radiation. *Journal
 609 of Geophysical Research*, 64(11):1683–1689.
- 610 Vernov, S. and Chudakov, A. (1960). Investigation of radiation in outer space. In
 611 *International Cosmic Ray Conference*, volume 3, page 19.
- 612 Walker, A. D. M. (1993). *Plasma waves in the magnetosphere*, volume 24. Springer
 613 Science & Business Media.